Eur. Phys. J. C 32, 475–492 (2004)
Digital Object Identifier (DOI) 10.1140/epjc/s2003-01469-8

THE EUROPEAN PHYSICAL JOURNAL C

Searches for invisibly decaying Higgs bosons with the DELPHI detector at LEP

The DELPHI Collaboration

J. Abdallah[25], P. Abreu[22], W. Adam[51], P. Adzic[11], T. Albrecht[17], T. Alderweireld[2], R. Alemany-Fernandez[8], T. Allmendinger[17], P.P. Allport[23], U. Amaldi[29], N. Amapane[45], S. Amato[48], E. Anashkin[36], A. Andreazza[28], S. Andringa[22], N. Anjos[22], P. Antilogus[25], W-D. Apel[17], Y. Arnoud[14], S. Ask[26], B. Asman[44], J.E. Augustin[25], A. Augustinus[8], P. Baillon[8], A. Ballestrero[46], P. Bambade[20], R. Barbier[27], D. Bardin[16], G. Barker[17], A. Baroncelli[39], M. Battaglia[8], M. Baubillier[25], K-H. Becks[53], M. Begalli[6], A. Behrmann[53], E. Ben-Haim[20], N. Benekos[32], A. Benvenuti[5], C. Berat[14], M. Berggren[25], L. Berntzon[44], D. Bertrand[2], M. Besancon[40], N. Besson[40], D. Bloch[9], M. Blom[31], M. Bluj[52], M. Bonesini[29], M. Boonekamp[40], P.S.L. Booth[23], G. Borisov[21], O. Botner[49], B. Bouquet[20], T.J.V. Bowcock[23], I. Boyko[16], M. Bracko[43], R. Brenner[49], E. Brodet[35], P. Bruckman[18], J.M. Brunet[7], L. Bugge[33], P. Buschmann[53], M. Calvi[29], T. Camporesi[8], V. Canale[38], F. Carena[8], N. Castro[22], F. Cavallo[5], M. Chapkin[42], Ph.Charpentier[8], P. Checchia[36], R. Chierici[8], P. Chliapnikov[42], J. Chudoba[8], S.U. Chung[8], K. Cieslik[18], P. Collins[8], R. Contri[13], G. Cosme[20], F. Cossutti[47], M.J. Costa[50], D. Crennell[37], J. Cuevas[34], J.D'Hondt[2], J. Dalmau[44], T.da Silva[48], W. Da Silva[25], G. Della Ricca[47], A. De Angelis[47], W. De Boer[17], C. De Clercq[2], B. De Lotto[47], N. De Maria[45], A. De Min[36], L.de Paula[48], L. Di Ciaccio[38], A. Di Simone[39], K. Doroba[52], J. Drees[53,8], M. Dris[32], G. Eigen[4], T. Ekelof[49], M. Ellert[49], M. Elsing[8], M.C. Espirito Santo[22], G. Fanourakis[11], D. Fassouliotis[11,3], M. Feindt[17], J. Fernandez[41], A. Ferrer[50], F. Ferro[13], U. Flagmeyer[53], H. Foeth[8], E. Fokitis[32], F. Fulda-Quenzer[20], J. Fuster[50], M. Gandelman[48], C. Garcia[50], Ph.Gavillet[8], E. Gazis[32], R. Gokieli[8,52], B. Golob[43], G. Gomez-Ceballos[41], P. Goncalves[22], E. Graziani[39], G. Grosdidier[20], K. Grzelak[52], J. Guy[37], C. Haag[17], A. Hallgren[49], K. Hamacher[53], K. Hamilton[35], S. Haug[33], F. Hauler[17], V. Hedberg[26], M. Hennecke[17], H. Herr[8], J. Hoffman[52], S-O. Holmgren[44], P.J. Holt[8], M.A. Houlden[23], K. Hultqvist[44], J.N. Jackson[23], G. Jarlskog[26], P. Jarry[40], D. Jeans[35], E.K. Johansson[44], P.D. Johansson[44], P. Jonsson[27], C. Joram[8], L. Jungermann[17], F. Kapusta[25], S. Katsanevas[27], E. Katsoufis[32], G. Kernel[43], B.P. Kersevan[8,43], U. Kerzel[17], A. Kiiskinen[15], B.T. King[23], N.J. Kjaer[8], P. Kluit[31], P. Kokkinias[11], C. Kourkoumelis[3], O. Kouznetsov[16], Z. Krumstein[16], M. Kucharczyk[18], J. Lamsa[1], G. Leder[51], F. Ledroit[14], L. Leinonen[44], R. Leitner[30], J. Lemonne[2], V. Lepeltier[20], T. Lesiak[18], W. Liebig[53], D. Liko[51], A. Lipniacka[44], J.H. Lopes[48], J.M. Lopez[34], D. Loukas[11], P. Lutz[40], L. Lyons[35], J. MacNaughton[51], A. Malek[53], S. Maltezos[32], F. Mandl[51], J. Marco[41], R. Marco[41], B. Marechal[48], M. Margoni[36], J-C. Marin[8], C. Mariotti[8], A. Markou[11], C. Martinez-Rivero[41], J. Masik[12], N. Mastroyiannopoulos[11], F. Matorras[41], C. Matteuzzi[29], F. Mazzucato[36], M. Mazzucato[36], R. Mc Nulty[23], C. Meroni[28], E. Migliore[45], W. Mitaroff[51], U. Mjoernmark[26], T. Moa[44], M. Moch[17], K. Moenig[8,10], R. Monge[13], J. Montenegro[31], D. Moraes[48], S. Moreno[22], P. Morettini[13], U. Mueller[53], K. Muenich[53], M. Mulders[31], L. Mundim[6], W. Murray[37], B. Muryn[19], G. Myatt[35], T. Myklebust[33], M. Nassiakou[11], F. Navarria[5], K. Nawrocki[52], R. Nicolaidou[40], M. Nikolenko[16,9], A. Oblakowska-Mucha[19], V. Obraztsov[42], A. Olshevski[16], A. Onofre[22], R. Orava[15], K. Osterberg[15], A. Ouraou[40], A. Oyanguren[50], M. Paganoni[29], S. Paiano[5], J.P. Palacios[23], H. Palka[18], Th.D. Papadopoulou[32], L. Pape[8], C. Parkes[24], F. Parodi[13], U. Parzefall[8], A. Passeri[39], O. Passon[53], L. Peralta[22], V. Perepelitsa[50], A. Perrotta[5], A. Petrolini[13], J. Piedra[41], L. Pieri[39], F. Pierre[40], M. Pimenta[22], E. Piotto[8], T. Podobnik[43], V. Poireau[8], M.E. Pol[6], G. Polok[18], P. Poropat[47], V. Pozdniakov[16], N. Pukhaeva[2,16], A. Pullia[29], J. Rames[12], L. Ramler[17], A. Read[33], P. Rebecchi[8], J. Rehn[17], D. Reid[31], R. Reinhardt[53], P. Renton[35], F. Richard[20], J. Ridky[12], M. Rivero[41], D. Rodriguez[41], A. Romero[45], P. Ronchese[36], P. Roudeau[20], T. Rovelli[5], V. Ruhlmann-Kleider[40], D. Ryabtchikov[42], A. Sadovsky[16], L. Salmi[15], J. Salt[50], A. Savoy-Navarro[25], U. Schwickerath[8], A. Segar[35], R. Sekulin[37], M. Siebel[53], A. Sisakian[16], G. Smadja[27], O. Smirnova[26], A. Sokolov[42], A. Sopczak[21], R. Sosnowski[52], T. Spassov[8], M. Stanitzki[17], A. Stocchi[20], J. Strauss[51], B. Stugu[4], M. Szczekowski[52], M. Szeptycka[52], T. Szumlak[19], T. Tabarelli[29], A.C. Taffard[23], F. Tegenfeldt[49], J. Timmermans[31], L. Tkatchev[16], M. Tobin[23], S. Todorovova[12], B. Tome[22], A. Tonazzo[29], P. Tortosa[50], P. Travnicek[12], D. Treille[8], G. Tristram[7], M. Trochimczuk[52], C. Troncon[28], M-L. Turluer[40], I.A. Tyapkin[16], P. Tyapkin[16], S. Tzamarias[11], V. Uvarov[42], G. Valenti[5], P. Van Dam[31], J. Van Eldik[8], A. Van Lysebetten[2], N.van Remortel[2], I. Van Vulpen[8], G. Vegni[28], F. Veloso[22], W. Venus[37], P. Verdier[27], V. Verzi[38], D. Vilanova[40], L. Vitale[47], V. Vrba[12], H. Wahlen[53], A.J. Washbrook[23], C. Weiser[17], D. Wicke[8], J. Wickens[2], G. Wilkinson[35], M. Winter[9], M. Witek[18], O. Yushchenko[42], A. Zalewska[18], P. Zalewski[52], D. Zavrtanik[43], V. Zhuravlov[16], N.I. Zimin[16], A. Zintchenko[16], M. Zupan[11]

[1] Department of Physics and Astronomy, Iowa State University, Ames IA 50011-3160, USA
[2] Physics Department, Universiteit Antwerpen, Universiteitsplein 1, 2610 Antwerpen, Belgium
and IIHE, ULB-VUB, Pleinlaan 2, 1050 Brussels, Belgium
and Faculté des Sciences, Univ. de l'Etat Mons, Av. Maistriau 19, 7000 Mons, Belgium
[3] Physics Laboratory, University of Athens, Solonos Str. 104, 10680 Athens, Greece
[4] Department of Physics, University of Bergen, Allégaten 55, 5007 Bergen, Norway
[5] Dipartimento di Fisica, Università di Bologna and INFN, Via Irnerio 46, 40126 Bologna, Italy
[6] Centro Brasileiro de Pesquisas Físicas, rua Xavier Sigaud 150, 22290 Rio de Janeiro, Brazil
and Depto. de Física, Pont. Univ. Católica, C.P. 38071 22453 Rio de Janeiro, Brazil
and Inst. de Física, Univ. Estadual do Rio de Janeiro, rua São Francisco Xavier 524, Rio de Janeiro, Brazil
[7] Collège de France, Lab. de Physique Corpusculaire, IN2P3-CNRS, 75231 Paris Cedex 05, France
[8] CERN, 1211 Geneva 23, Switzerland
[9] Institut de Recherches Subatomiques, IN2P3 - CNRS/ULP - BP20, 67037 Strasbourg Cedex, France
[10] Now at DESY-Zeuthen, Platanenallee 6, 15735 Zeuthen, Germany
[11] Institute of Nuclear Physics, N.C.S.R. Demokritos, P.O. Box 60228, 15310 Athens, Greece
[12] FZU, Inst. of Phys. of the C.A.S. High Energy Physics Division, Na Slovance 2, 180 40, Praha 8, Czech Republic
[13] Dipartimento di Fisica, Università di Genova and INFN, Via Dodecaneso 33, 16146 Genova, Italy
[14] Institut des Sciences Nucléaires, IN2P3-CNRS, Université de Grenoble 1, 38026 Grenoble Cedex, France
[15] Helsinki Institute of Physics, P.O. Box 64, 00014 University of Helsinki, Finland
[16] Joint Institute for Nuclear Research, Dubna, Head Post Office, P.O. Box 79, 101 000 Moscow, Russian Federation
[17] Institut für Experimentelle Kernphysik, Universität Karlsruhe, Postfach 6980, 76128 Karlsruhe, Germany
[18] Institute of Nuclear Physics,Ul. Kawiory 26a, 30055 Krakow, Poland
[19] Faculty of Physics and Nuclear Techniques, University of Mining and Metallurgy, 30055 Krakow, Poland
[20] Université de Paris-Sud, Lab. de l'Accélérateur Linéaire, IN2P3-CNRS, Bât. 200, 91405 Orsay Cedex, France
[21] School of Physics and Chemistry, University of Lancaster, Lancaster LA1 4YB, UK
[22] LIP, IST, FCUL - Av. Elias Garcia, 14-1^{o}, 1000 Lisboa Codex, Portugal
[23] Department of Physics, University of Liverpool, P.O. Box 147, Liverpool L69 3BX, UK
[24] Dept. of Physics and Astronomy, Kelvin Building, University of Glasgow, Glasgow G12 8QQ
[25] LPNHE, IN2P3-CNRS, Univ. Paris VI et VII, Tour 33 (RdC), 4 place Jussieu, 75252 Paris Cedex 05, France
[26] Department of Physics, University of Lund, Sölvegatan 14, 223 63 Lund, Sweden
[27] Université Claude Bernard de Lyon, IPNL, IN2P3-CNRS, 69622 Villeurbanne Cedex, France
[28] Dipartimento di Fisica, Università di Milano and INFN-MILANO, Via Celoria 16, 20133 Milan, Italy
[29] Dipartimento di Fisica, Univ. di Milano-Bicocca and INFN-MILANO, Piazza della Scienza 2, 20126 Milan, Italy
[30] IPNP of MFF, Charles Univ., Areal MFF, V Holesovickach 2, 180 00, Praha 8, Czech Republic
[31] NIKHEF, Postbus 41882, 1009 DB Amsterdam, The Netherlands
[32] National Technical University, Physics Department, Zografou Campus, 15773 Athens, Greece
[33] Physics Department, University of Oslo, Blindern, 0316 Oslo, Norway
[34] Dpto. Fisica, Univ. Oviedo, Avda. Calvo Sotelo s/n, 33007 Oviedo, Spain
[35] Department of Physics, University of Oxford, Keble Road, Oxford OX1 3RH, UK
[36] Dipartimento di Fisica, Università di Padova and INFN, Via Marzolo 8, 35131 Padua, Italy
[37] Rutherford Appleton Laboratory, Chilton, Didcot OX11 OQX, UK
[38] Dipartimento di Fisica, Università di Roma II and INFN, Tor Vergata, 00173 Rome, Italy
[39] Dipartimento di Fisica, Università di Roma III and INFN, Via della Vasca Navale 84, 00146 Rome, Italy
[40] DAPNIA/Service de Physique des Particules, CEA-Saclay, 91191 Gif-sur-Yvette Cedex, France
[41] Instituto de Fisica de Cantabria (CSIC-UC), Avda. los Castros s/n, 39006 Santander, Spain
[42] Inst. for High Energy Physics, Serpukov P.O. Box 35, Protvino, (Moscow Region), Russian Federation
[43] J. Stefan Institute, Jamova 39, 1000 Ljubljana, Slovenia
and Laboratory for Astroparticle Physics, Nova Gorica Polytechnic, Kostanjeviska 16a, 5000 Nova Gorica, Slovenia,
and Department of Physics, University of Ljubljana, 1000 Ljubljana, Slovenia
[44] Fysikum, Stockholm University, Box 6730, 113 85 Stockholm, Sweden
[45] Dipartimento di Fisica Sperimentale, Università di Torino and INFN, Via P. Giuria 1, 10125 Turin, Italy
[46] INFN,Sezione di Torino, and Dipartimento di Fisica Teorica, Università di Torino, Via P. Giuria 1, 10125 Turin, Italy
[47] Dipartimento di Fisica, Università di Trieste and INFN, Via A. Valerio 2, 34127 Trieste, Italy
and Istituto di Fisica, Università di Udine, 33100 Udine, Italy
[48] Univ. Federal do Rio de Janeiro, C.P. 68528 Cidade Univ., Ilha do Fundão 21945-970 Rio de Janeiro, Brazil
[49] Department of Radiation Sciences, University of Uppsala, P.O. Box 535, 751 21 Uppsala, Sweden
[50] IFIC, Valencia-CSIC, and D.F.A.M.N., U. de Valencia, Avda. Dr. Moliner 50, 46100 Burjassot (Valencia), Spain
[51] Institut für Hochenergiephysik, Österr. Akad. d. Wissensch., Nikolsdorfergasse 18, 1050 Vienna, Austria
[52] Inst. Nuclear Studies and University of Warsaw, Ul. Hoza 69, 00681 Warsaw, Poland
[53] Fachbereich Physik, University of Wuppertal, Postfach 100 127, 42097 Wuppertal, Germany

Received: 2 September 2003 / Revised version: 10 November 2003 /
Published online: 15 January 2004 – © Springer-Verlag / Società Italiana di Fisica 2003

Abstract. Searches for HZ production with the Higgs boson decaying into an invisible final state were performed using the data collected by the DELPHI experiment at centre-of-mass energies between 188 GeV and 209 GeV. Both hadronic and leptonic final states of the Z boson were analysed. In addition to the search for a heavy Higgs boson, a dedicated search for a light Higgs boson down to 40 GeV/c^2 was performed. No signal was found. Assuming the Standard Model HZ production cross-section, the mass limit for invisibly decaying Higgs bosons is 112.1 GeV/c^2 at 95% confidence level. An interpretation in the Minimal Supersymmetric extension of the Standard Model (MSSM) and in a Majoron model is also given.

1 Introduction

The data collected by DELPHI have been searched for the presence of a Higgs boson produced in association with a Z, in $e^+e^- \to HZ$, but which decays to stable non-interacting particles. The process is illustrated in Fig. 1. Such invisible Higgs boson decays can occur in Supersymmetry, where the Higgs could decay into a pair of neutralinos $\tilde{\chi}_1^0$ [1–3]. In such models $\tilde{\chi}_1^0$ is assumed to be the lightest supersymmetric particle and therefore assumed to be stable. It is weakly interacting with ordinary matter. Invisible Higgs decays also occur in Majoron models [4–6] with the Higgs decaying into two Majorons. The results of the search described in this article are valid more generally in models with stable Higgs bosons that do not interact in the detector.

Similar searches have been previously performed by DELPHI [7,8] using data at lower centre-of-mass energies and by other LEP experiments [9,10]. In this paper searches are presented in four different final states, where the Z decays either into a $q\bar{q}$, e^+e^-, $\mu^+\mu^-$ or $\tau^+\tau^-$ pair.

The paper is organised as follows: First the analyses in the hadronic channel are addressed separately in high and low mass ranges. Then we describe the analyses in the leptonic channels which cover μ, e, and τ final states. Next, the results are summarised and 95% Confidence Level (CL) limits are calculated. The limits are then reinterpreted in the framework of the Minimal Supersymmetric extension of the Standard Model (MSSM) and in a Majoron model.

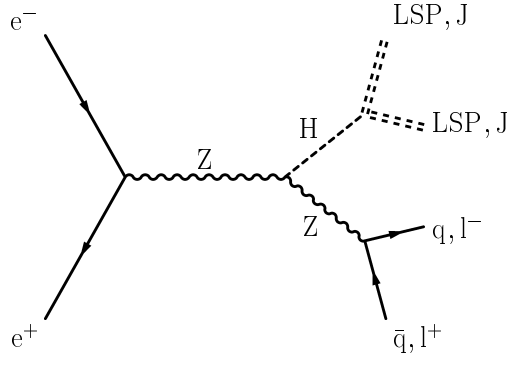

Fig. 1. Feynman diagram describing the HZ production with the Higgs boson decaying into invisible particles, e.g. the lightest supersymmetric particle (LSP) or a Majoron (J) in models with an extended Higgs sector

2 The DELPHI detector and the data set

The analyses were mainly based on the information from the tracking system, the calorimeters, the muon chambers, and the photon veto counters of the DELPHI detector. The scintillation counters veto photons in blind regions of the electromagnetic calorimeters at polar angles near 40°, 90° and 140°. The DELPHI detector and its performance are described in detail in [11,12].

The data set analysed in this paper was taken in the years 1998 to 2000. In 1998 and 1999, data were recorded at centre-of-mass energies 188.7, 191.6, 195.6, 199.6 and 201.7 GeV. In 2000 the LEP energy was varied from 199.7 to 208.4 GeV and the data taken at energies below and above 205.8 GeV were analysed as two independent subsamples, with mean energies of 205.0 and 206.7 GeV. At the end of the year 2000 data taking, one of the twelve sectors of the Time Projection Chamber (TPC) became non-operational. Data taken afterwards were then treated as a separate sample, with a mean centre-of-mass energy of 206.3 GeV. In the following, these three subsamples of the 2000 data set will be referred to by the energy of each simulation for the corresponding data, namely 205.0, 206.5 and 206.5U. The simulation of the last data taking period (206.5U) included the effect of the missing TPC sector in the detector setup and the changes in the reconstruction software to partly recover this loss.

For the analysis of the hadronic and leptonic channels different criteria are required on the detector status during data taking. As a result the total data sets correspond to 589 $pb^{-1}$and 571 pb^{-1}, respectively. For the simulation of the signal the `HZHA` generator [13] was used for the four final states. For all the years of data-taking simulated signal samples with 5000 events per mass point and channel were generated with the Higgs masses from 40 to 90 GeV/c^2 in 5 GeV/c^2 steps, from 90 to 115.0 GeV/c^2 in 2.5 GeV/c^2 steps and at 120 GeV/c^2 .

The background processes $e^+e^- \to q\bar{q}(n\gamma)$ and $\mu^+\mu^-(n\gamma)$ were generated using the `KK2F` generator [14] and the background process $\tau^+\tau^-(n\gamma)$ was generated using the `KORALZ` generator [15]. The processes which lead to charged and neutral current four-fermion final states were generated with the `WPHACT` generator [16]. The `PYTHIA` generator [17] was used to describe the hadronic two-photon processes, and the `BDK` generator [18] was used to describe the leptonic two-photon processes. Finally, the `BHWIDE` generator [19] was used for the Bhabha processes. Both signal and back-

ground events were processed through the full DELPHI detector simulation [11]. The inoperative sector in the TPC is also taken into account in the corresponding simulation in the 206.5U data set.

3 The hadronic channel

The hadronic decay of the Z represents 70% of the HZ final states. The signature of an invisible Higgs boson decay is a pair of acoplanar and acollinear jets with a di-jet mass compatible with the Z mass and missing energy and momentum due to the invisibly decaying Higgs boson.

In order to obtain a good performance in the whole mass range, two overlapping mass windows were defined for each year of operation and the analyses were optimised for each window as defined in Table 1.

Table 1. Hadronic channel: Low and high Higgs boson mass ranges for three years of data-taking

Year	Low mass range (GeV/c^2)	High mass range (GeV/c^2)
1998	40–90	75–120
1999	40–100	75–120
2000	40–105	95–120

3.1 High mass analysis

The selection of HZ candidate events consists of several steps in order to suppress the bulk of the background. First, the events were clustered into jets using the DURHAM [20] algorithm. Then a preselection was applied to remove most of the two-photon background and a great part of the backgrounds due to four-fermion processes and to hadronic events with a radiative return to an on-shell Z. Then the final separation between the signal and the background channels was achieved through an Iterative Discriminant Analysis (IDA) [21]. The details of the preselection are:

- Anti-$\gamma\gamma$: Each event was required to have at least 9 charged particle tracks. Two of them must have transverse momentum greater than 2 GeV/c and impact parameters to the primary vertex less than 1 mm in the transverse plane and less than 3 mm along the beam axis. It was also required that the charged energy be greater than $0.16\sqrt{s}$. There should be no electromagnetic shower with more than $0.45\sqrt{s}$, the transverse energy[1] be greater than $0.15\sqrt{s}$ and the sum of the longitudinal momenta be greater than $0.25\sqrt{s}$.
- Anti-q$\bar{\text{q}}(n\gamma)$ and anti-WW: A cut in the $\theta_{\text{p}_{\text{mis}}}$ versus $\sqrt{s'}$ [22] plane was applied, required

$$40^\circ \leq \theta_{\text{p}_{\text{mis}}} \leq 140^\circ \quad \text{and} \quad \sqrt{\text{s}'} \geq 115\,\text{GeV},$$

where $\sqrt{s'}$ stands for the effective centre-of-mass energy after the initial state radiation of one or more photons and $\theta_{\text{p}_{\text{mis}}}$ is the polar angle of the missing momentum. In addition, it was required that less than $0.08\sqrt{s}$ was deposited in the STIC[2] [11], $\sqrt{s'}/\sqrt{\text{s}}$ was less than 0.96 and that the total electromagnetic energy within 30° of the beam directions was less than $0.16\sqrt{s}$. In order to suppress badly reconstructed events, candidates in which a jet pointed to the insensitive region between barrel and endcap detectors or where both jet axes were below 12° were rejected. A hermeticity veto algorithm [23] using the scintillator counters was applied to ensure that no photon escaped in the insensitive region of the electromagnetic calorimeter at polar angles near 40°, 90° and 140°. To suppress background from WW pair production, the energy of the most energetic particle was required to be less than $0.2\sqrt{s}$ and the transverse momentum of any particle in the jet with respect to its jet axis (forcing the event into a two-jet configuration) to be less than $0.05\sqrt{s}/c$. Finally, upon forcing the event into a three-jet configuration, it was required that every jet had at least one charged particle in order to suppress q$\bar{\text{q}}(n\gamma)$ events.

Twelve variables were used to construct an effective tagging variable in the framework of the IDA. In order to calculate these variables, the event was forced into two jets. The variables are:

- $E_\gamma/E_\gamma^{\text{Z}}$: the normalised energy of a photon assumed to have escaped in the beam direction, deduced from the polar angles of the two jet directions in the event. The photon energy was normalised to the energy expected for a photon recoiling against an on-shell Z.
- $\ln(p_{\text{T}}$ [GeV/c]): logarithm of the transverse momentum of the event.
- $E_{\text{vis}}/\sqrt{s}$: visible energy of the event, normalised to the centre-of-mass energy.
- $E_{\text{T}}/\sqrt{s}$: transverse energy of the event, normalised to the centre-of-mass energy.
- θ_{cone}: The minimum polar angle defining a cone in the positive and negative beam directions containing 6% of the total visible energy.
- $|\cos\theta_{p_{\text{mis}}}|$: cosine of the polar angle of the missing momentum.
- $E_{\text{isol}}/\sqrt{s}$: energy sum between the two cones, defined by half opening angles 5° and $\alpha_{\max}$ around the most isolated particle. The energy sum is then normalised to the centre-of-mass energy. The most isolated particle is defined as the particle with momentum above 2 GeV/c with the smallest energy sum in the double cone. In the momentum interval from 2 to 5 GeV/c, $\alpha_{\max}$ is set to 60° in order to maximise the sensitivity to isolated particles from tau decays in WW $\to$ q$\bar{\text{q}}'\tau\nu$ events. An opening angle of 25° is used for particles with momenta above 5 GeV/c.
- $p_{\text{isol}}/\sqrt{s}$: momentum of the most isolated particle, as defined above, normalised to the centre-of-mass energy.

[1] The transverse energy is the energy perpendicular to the beam axis, defined as $E_{\text{T}} = \sqrt{p_x^2 + p_y^2 + m^2}$.

[2] Small angle TIle Calorimeter, covering the very forward region.

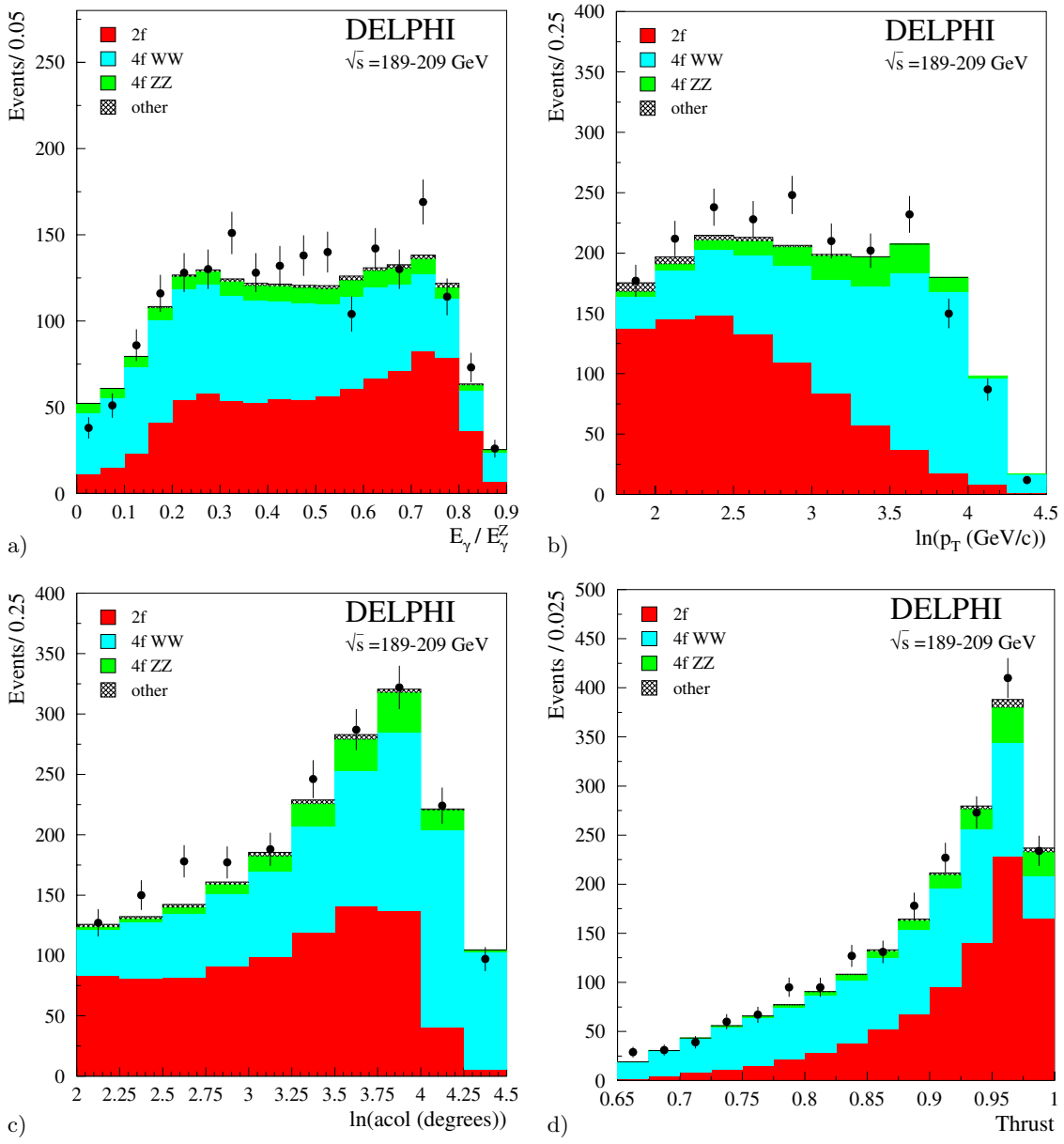

Fig. 2a–d. Hadronic channel high mass analysis: Distribution of the four IDA input variables after the final preselection as described in Sect. 3.1: **a** E_γ/E_γ^Z; **b** $\ln(p_T)$ in GeV/c; **c** ln(acollinearity) in degrees; **d** Thrust

– $\log_{10}$(scaled acoplanarity): The acoplanarity is defined as $180° - \Delta\phi$, where $\Delta\phi$ is the difference in azimuthal angle (in the plane perpendicular to the beam axis) between the two jets. In order to compensate for the geometrical instability of the acoplanarity for jets at low angles it was multiplied with the angle between the two jets.
– Thrust: thrust value of the event, computed in the rest frame of the visible system.
– ln(acollinearity): logarithm of the acollinearity (in degrees) of the two-jet system.
– $\ln(\max(p_T \ \ [\mathrm{GeV}/c])_{\mathrm{jet}})$: highest transverse momentum of the jet-particles, defined by the transverse momentum of any particle in the jet with respect to the jet axis.

The cuts listed in Table 2 were applied in the tails of the distribution of these variables in order to concentrate on the signal region and to avoid long tails in the input variables for the IDA. In addition to the cuts listed in Table 2, the number of electrons or muons identified by the standard DELPHI algorithms [11] was required to be less than three. The agreement between data and simulation is shown in Table 3 and Fig. 2. There is a small excess in data over expected background, which is not concentrated in one bin.

The IDA is a modified Fisher Discriminant Analysis, the two main differences are the introduction of a non-linear discriminant function and iterations in order to enhance the separation of signal and background. Two IDA steps were performed, with a cut after the first IDA it-

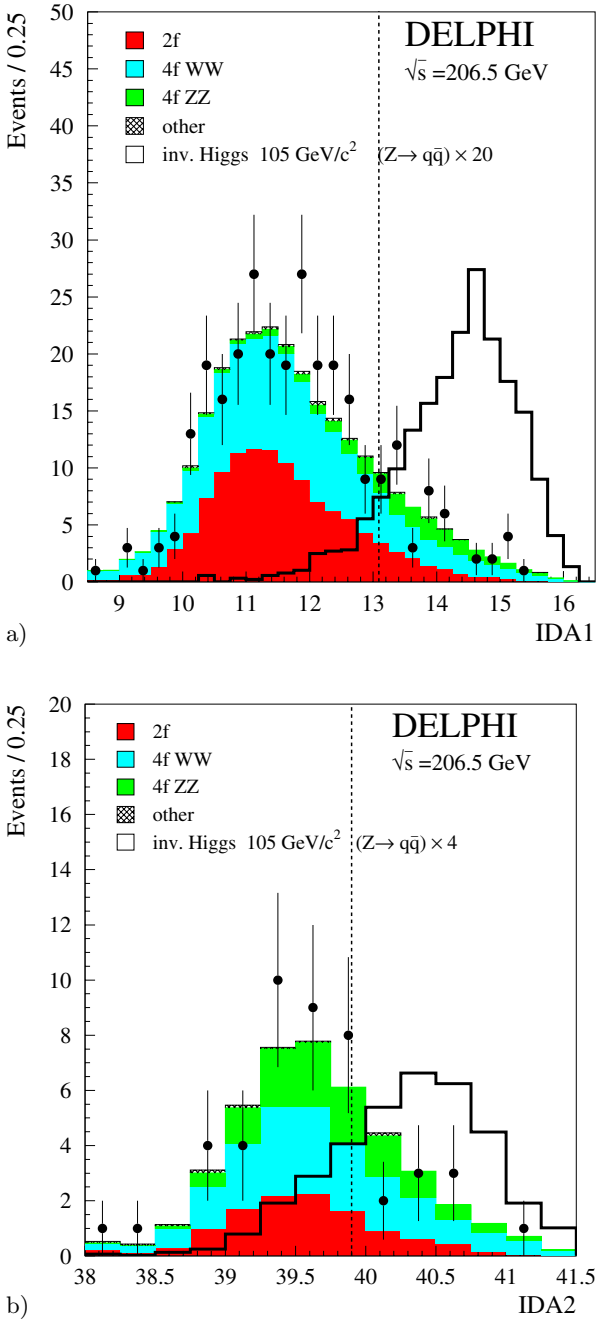

Fig. 3a,b. Hadronic channel high mass analysis: Distributions for the IDA variables after first **a** and second IDA step **b** at $\sqrt{s} = 206.5$ GeV. The dashed line indicates the cut on the IDA variable. The white histogram shows the expectation of a 105 GeV/c^2 Higgs signal where the signal rate is enhanced by a factor 20 for **a** and 4 for **b**

eration keeping 90% of the signal efficiency. In order to have two independent samples for the derivation of the IDA function and for the expected performance, the signal and background samples were divided in two equally sized samples. As an illustration, the distributions of the two IDA variables at $\sqrt{s} = 206.5$ GeV are shown in Fig. 3. The slight disagreement in the rates observed at the pre-

Table 2. Tail cuts used in the high mass hadronic analysis. The variables are described in detail in Sect. 3.1

Variable	lower cut	upper cut
E_γ/E_γ^Z	–	0.90
$\ln(p_T$ [GeV/c])	1.75	4.5
$E_T/\sqrt{s}$	0.15	0.6
$p_{isol}/\sqrt{s}$	0.008	0.18
$\log_{10}$(scaled acoplanarity)	0.3	2.5
Thrust	0.65	1.0
ln(acollinearity)	2.0	4.5
$\ln(\max(p_T)$ [GeV/$c]_{jet}$)	−0.5	2.50

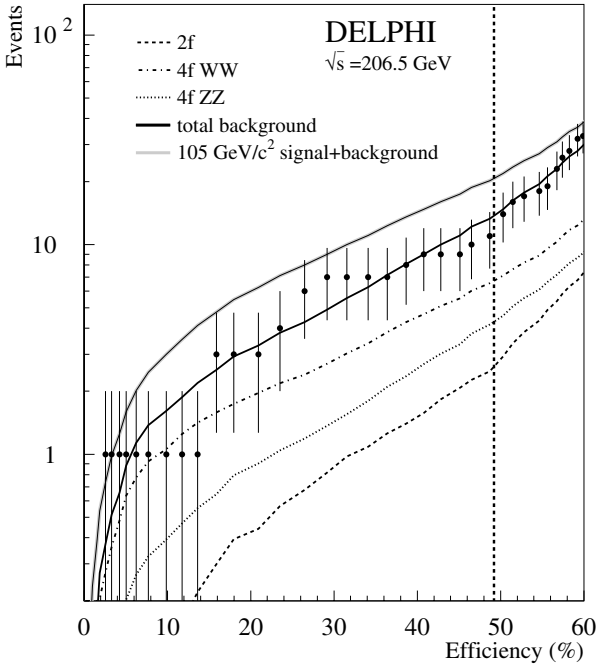

Fig. 4. Hadronic channel high mass analysis: Data and expected background for the 206.5 GeV centre-of-mass energy as a function of the efficiency for an invisibly decaying Higgs boson of 105 GeV/c^2. The lines represent the most important backgrounds with the solid black line showing the sum of all the background processes. In addition the grey line shows the expectation for a 105 GeV/c^2 Higgs signal added on top of the background. The vertical dashed line indicates the final cut chosen to maximise the sensitivity

selection level is effectively removed by the IDA analysis, since it is concentrated mostly outside the signal region.

The observed and expected rates at $\sqrt{s} = 206.5$ GeV are shown in Fig. 4 as a function of the efficiency to detect a 105 GeV/c^2 Higgs boson when varying the cut on the second IDA variable. The final cut on the second IDA variable was determined by maximising the expected exclusion power. This was done separately for each centre-of-mass energy to optimise the analysis for a 85 GeV/c^2 Higgs boson at 188.6 GeV, for a 95 GeV/c^2 Higgs boson at 191.6 and 195.6 GeV, for a 100 GeV/c^2 Higgs at 199.5 and 201.6 GeV

Table 3. Comparison of simulation and data after the different steps of the preselection in the high mass hadronic analysis. The listed errors are from Monte Carlo statistics only

$\sqrt{s}$	Anti-$\gamma\gamma$		Anti-$q\bar{q}(n\gamma)$ & anti-WW		Tail cuts	
(GeV)	Data	MC	Data	MC	Data	MC
188.6	15115	14967.0 ± 8.1	1578	1565.2 ± 6.0	494	485.9 ± 3.2
191.6	2394	2351.8 ± 1.3	258	249.9 ± 0.9	88	79.0 ± 0.5
195.5	7040	6782.4 ± 3.7	739	734.9 ± 2.8	242	242.0 ± 1.4
199.5	7296	7168.9 ± 3.9	784	795.4 ± 2.8	295	264.4 ± 1.6
201.6	3557	3407.8 ± 1.9	396	382.9 ± 1.3	152	130.6 ± 0.7
205.0	6272	6011.6 ± 3.7	678	686.2 ± 2.4	240	239.2 ± 1.3
206.5	6772	6697.0 ± 4.5	798	768.5 ± 2.9	283	268.2 ± 1.6
206.5U	4472	4560.4 ± 3.9	534	541.5 ± 2.6	202	190.7 ± 1.5

and for a $105\,\mathrm{GeV}/c^2$ Higgs at 205.0, 206.5 GeV and 206.5U GeV. We assume Standard Model production cross-section and a branching ratio of 100% into invisible final states. For example, in Fig. 4 the cut on the second IDA is indicated by the dashed vertical line. The final number of selected events in data and Monte Carlo simulations is given in Table 7.

3.2 Low-mass analysis

For the low-mass analysis, the preselection was adapted for the different event shape and kinematics. In the anti-$q\bar{q}(n\gamma)$ and anti-WW selection the cut in the $\theta_{p_{mis}}$ vs $\sqrt{s'}$ plane and the cut on $\sqrt{s'}/\sqrt{s}$ were removed in order to increase the signal efficiency. This was possible because the signal events have a much smaller amount of missing energy than the events in the high-mass range. Some tail cuts were also slightly changed as shown in Table 4 and a cut requiring the visible mass to be at least 20% of $\sqrt{s}$ was added. Figure 5 and Table 5 show the agreement of data and background at the preselection level. Fig. 5a shows an excess of data over the expected background near $E_\gamma/E_\gamma^Z = 1$ due to an underestimation of the two-fermion processes. This region is effectively removed by the IDA analysis.

The low-mass analysis also used two IDA steps in order to obtain optimal signal to background discrimination. The distributions of the two IDA variables at $\sqrt{s}$=195.5 GeV are shown in Fig. 6. The observed and expected rates at $\sqrt{s} = 195.5$ GeV are shown in Fig. 7 as a function of the efficiency to detect a Higgs boson when varying the cut on the second IDA variable. The cut on the second IDA variable was again determined separately for each centre-of-mass energy as described above. It was optimised for a $60\,\mathrm{GeV}/c^2$ Higgs boson mass at all energies. The final number of selected events in data and Monte Carlo simulations is given in Table 8.

Table 4. Tail cuts used in the low mass hadronic analysis. The variables are described in detail in Sect. 3.1

Variable	lower cut	upper cut
E_γ/E_γ^Z	–	1.20
$E_T/\sqrt{s}$	–	0.6
$p_{isol}/\sqrt{s}$	–	0.18
$\log_{10}$(scaled acoplanarity)	1.0	2.5
ln(acollinearity)	2.25	4.5

3.3 Mass reconstruction

The recoil mass to the di-jet system corresponds to the mass of the invisible Higgs boson. It was calculated with a Z mass constraint for the measured di-jet system from the visible energy E_{vis} and the visible mass m_{vis}. The following expression was used

$$m_{inv} = \sqrt{\left(\sqrt{s} - \frac{m_Z E_{vis}}{m_{vis}}\right)^2 - \left(\frac{m_Z p_{mis}}{m_{vis}}\right)^2},$$

where p_{mis} is the missing momentum and m_Z is the Z mass. The recoil mass distribution after the final selection for the high-mass analysis is shown in Fig. 8. For the low-mass region this method was also used. In cases where the fit obtained negative mass squares the standard missing mass calculation $\sqrt{E_{mis}^2 - p_{mis}^2}$ was used, where $E_{mis} = \sqrt{s} - E_{vis}$. The recoil mass distribution for the low mass analysis is shown in Fig. 9.

3.4 Systematic errors

Several sources of systematics have been considered, first the effect of modelling the $q\bar{q}(n\gamma)$ background from different generators was studied by replacing the `KK2F` generator with the `ARIADNE` generator [24] at 206.5 GeV. The results were identical within statistical errors. The error of the luminosity is conservatively taken to be ±0.5%. The process $e^+e^- \to q\bar{q}e\bar{\nu}$ provides about a fifth of the background and the uncertainty on the cross-section of this process is taken to be ±5% [25]. This leads to an ±1% uncertainty of the background. In order to see the influence of the jet clustering algorithm the DURHAM algorithm was replaced by the LUCLUS algorithm [26]. This results in an uncertainty on the background estimation and the signal efficiency in

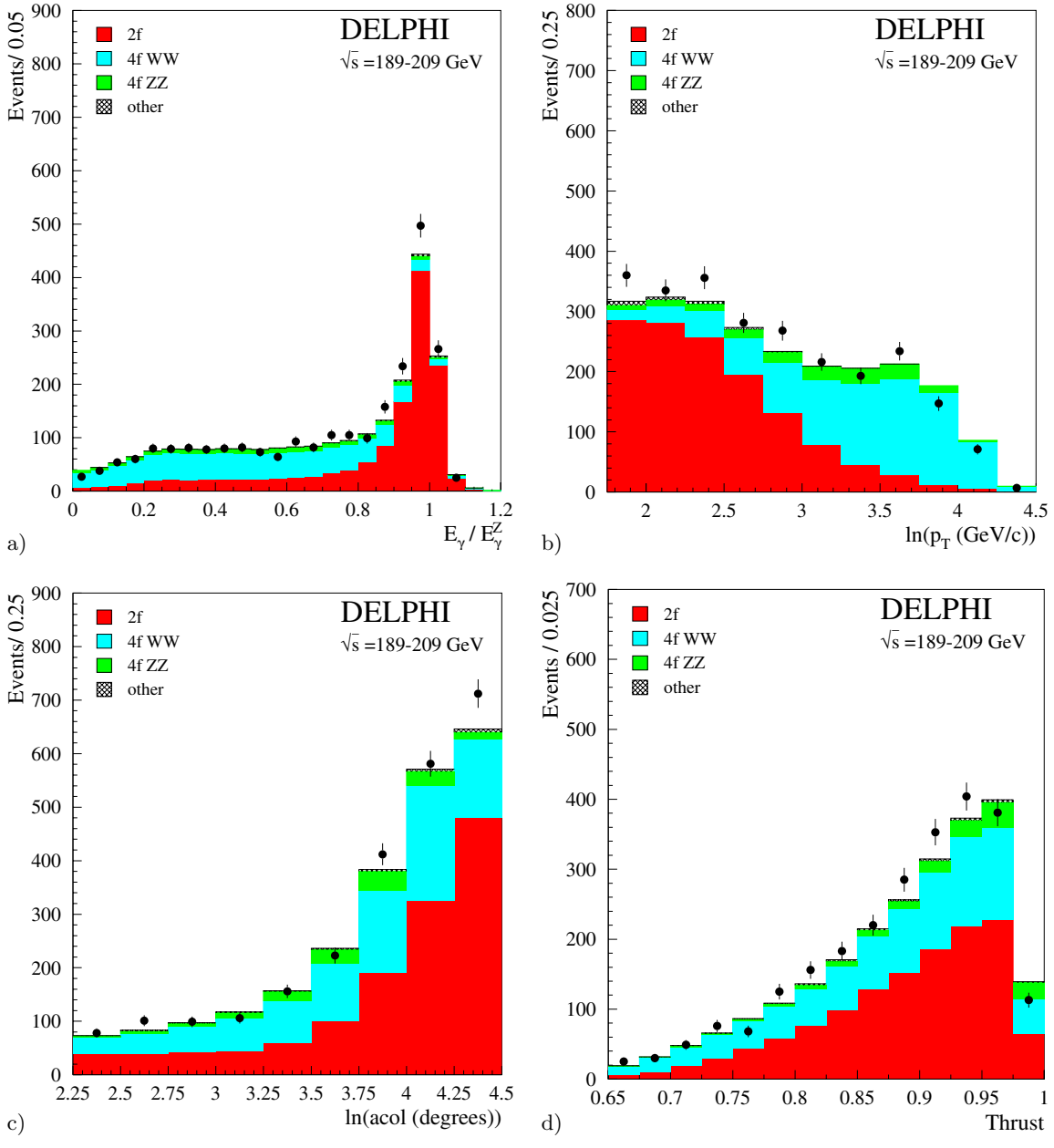

Fig. 5a–d. Hadronic channel low mass analysis: Distribution of the four IDA input variables after the final preselection as described in Sect. 3.1: **a** E_γ/E_γ^Z; **b** $\ln(p_T)$ in GeV/c; **c** ln(acollinearity) in degrees; **d** Thrust

the order of ±1% for the high mass regime and an error in the order of ±2.5% for the low mass regime.

The data and Monte Carlo simulation were found to be in good overall agreement. However, since we are searching for events with a large amount of missing energy, we become sensitive to the tails of the distributions from the expected Standard Model background events. When analysing the same topology for the measurement of the Z pair production cross-section [27], it was found that the small disagreement in the tails can be cured if the particle multiplicities of data and Monte Carlo simulation are brought into agreement. In order not to bias the present analysis, where the disagreements in the tails could come from new physics, the tuning of the particle multiplicities was performed with $\mathrm{Z} \to \mathrm{q\bar{q}}$ events taken at $\sqrt{s} = 91.1\,\mathrm{GeV}$ for each year of data taking. The particle multiplicities were estimated separately for the barrel ($\cos\theta \leq 0.7$) and the forward region ($\cos\theta > 0.7$) and for different momentum bins and separately for neutral and charged particles. For each of these classes of multiplicities a separate correction factor P was calculated using

$$P = \frac{< N_{\mathrm{data}} > - < N_{\mathrm{MC}} >}{< N_{\mathrm{MC}} >},$$

where $< N_{\mathrm{data}} >$ is the mean value of the particle multiplicity in the data and $< N_{\mathrm{MC}} >$ is the corresponding simulated value. These correction factors are of the order of a few percent in the barrel region, they tend to be

Table 5. Comparison of simulation and data after the different steps of the preselection in the low mass hadronic analysis. The errors given are from Monte Carlo statistics only

$\sqrt{s}$	Anti-$\gamma\gamma$		Anti-$q\bar{q}(n\gamma)$ & anti-WW		Tail cuts	
(GeV)	Data	MC	Data	MC	Data	MC
188.6	15115	14967.0 ± 8.1	6604	6735.2 ± 11.0	622	652.0 ± 3.9
191.6	2394	2351.8 ± 1.3	1013	1051.2 ± 1.7	112	103.0 ± 0.6
195.5	7040	6782.4 ± 3.7	2939	3003.0 ± 4.8	322	301.3 ± 1.8
199.5	7296	7168.9 ± 3.9	3122	3117.7 ± 5.0	338	315.1 ± 1.8
201.6	3557	3407.8 ± 1.9	1551	1495.9 ± 2.4	168	152.1 ± 0.8
205.0	6272	6011.6 ± 3.7	2617	2614.9 ± 4.3	344	307.3 ± 1.6
206.5	6772	6697.0 ± 4.5	2885	2909.0 ± 5.2	305	293.6 ± 1.7
206.5U	4472	4560.4 ± 3.9	1878	1982.5 ± 4.7	257	237.5 ± 1.7

Table 6. Comparison of simulation and data at preselection level in the three leptonic channels. The errors reflect the Monte Carlo statistics only

$\sqrt{s}$	$\mu^+\mu^-$		e^+e^-		$\tau^+\tau^-$	
(GeV)	Data	MC	Data	MC	Data	MC
188.6	64	49.7 ± 0.8	314	298.0 ± 7.1	124	148.2 ± 3.7
191.6	10	7.9 ± 0.1	46	45.5 ± 1.1	18	22.4 ± 0.8
195.5	19	22.5 ± 0.3	132	125.5 ± 3.1	78	62.2 ± 2.1
199.5	24	24.8 ± 0.3	149	134.6 ± 3.2	81	74.9 ± 1.8
201.6	17	12.1 ± 0.2	60	65.9 ± 1.6	34	32.1 ± 1.1
205.0	11	20.5 ± 0.3	98	114.2 ± 2.7	70	55.3 ± 1.0
206.5	26	23.1 ± 0.3	110	129.5 ± 2.2	76	71.9 ± 1.1
206.5U	6	14.6 ± 0.2	79	76.3 ± 1.9	48	40.3 ± 1.3

larger in the forward region and are also larger for neutral than for charged particles. The correction factors obtained were then applied to the high energy LEP2 Monte Carlo simulation on an event by event basis. The factor P was used as a probability to modify the particle multiplicities in the Monte Carlo simulation and related variables were recalculated. If P was less than zero, there were fewer particles in data than in Monte Carlo and the particles of the corresponding class were removed in the simulated events. For P greater than zero, particles have to be added to the simulated events. This was performed copying another particle of the same class and smearing its momentum by 2.5% in order not to affect the event jet topology. If there was no particle of the corresponding class, a particle of the adjacent class was taken and scaled to fit into this class. These modifications of the multiplicities in the Monte Carlo simulation were not used to change the analysis, but only to estimate the systematic errors. The effect on the final background estimation ranges from ±10.5% (1998), ±4.7% (1999) to ±10.6%(2000) for the high mass range analysis. For the low mass range the effects are smaller, they range from ±6.6% (1998), ±4.3% (1999) to ±5.6% (2000). This procedure also affects the signal efficiencies leading to a reduction of the relative signal efficiency of up to ±1.5%. The application of this method to the analysis variables leads to a better agreement of data at the preselection level as has been observed previously in the measurement of the Z pair production cross-section [27]. This leads to a better estimation of the systematic error on the simulated background. The total systematic error and statistical error from the limited MC statistics are combined in quadrature and given in Table 7 and Table 8.

4 Leptonic channels

The leptonic channel $H\ell^+\ell^-$ represents about 10% of the HZ final state. The experimental signature of the $HZ(Z \to \ell^+\ell^-)$ final states is a pair of acoplanar and acollinear leptons, with an invariant mass compatible with that of an on-shell Z boson.

The analysis contains a preselection for leptonic events. Then the search channel is defined by the lepton-type of the Z decay mode and for each decay mode specific selection cuts were applied. Two different sets of final cuts were used, depending on the reconstructed mass, defining the low-mass and high-mass ranges.

4.1 Leptonic preselection

To ensure a good detector performance the data corresponding to runs in which subdetectors were not fully operational were discarded. In particular it was required that the tracking subdetectors and calorimeters were fully operational and that the muon chambers were fully functional.

Table 7. Integrated luminosity, observed number of events, expected number of background events and signal efficiency ($100\,\mathrm{GeV}/c^2$ signal mass) for different energies. The last lines of each channel (206.5U) refers to the data taken with one TPC sector inoperative, which has been fully taken into account in the event simulations. Systematic and statistical errors are combined in quadrature

$\sqrt{s}$ (GeV)	Channel	Luminosity (pb^{-1})	Data	Expected background	Signal efficiency (%)
188.6	$q\bar{q}$	152.4	65	71.3 ± 7.7	40.9 ± 1.9
191.1	$q\bar{q}$	24.7	2	5.6 ± 0.3	39.6 ± 1.7
195.5	$q\bar{q}$	74.3	21	18.7 ± 1.0	50.8 ± 1.7
199.5	$q\bar{q}$	82.2	21	20.1 ± 1.0	51.9 ± 1.7
201.6	$q\bar{q}$	40.0	11	10.8 ± 0.5	50.7 ± 1.7
205.0	$q\bar{q}$	74.3	9	12.2 ± 1.3	36.4 ± 2.1
206.5	$q\bar{q}$	82.8	13	13.5 ± 1.5	37.0 ± 2.1
206.5U	$q\bar{q}$	58.0	11	8.4 ± 0.9	31.6 ± 2.1
188.6	$\mu^+\mu^-$	153.8	7	6.9 ± 0.6	44.0 ± 1.9
191.1	$\mu^+\mu^-$	24.5	4	1.1 ± 0.1	52.8 ± 1.6
195.5	$\mu^+\mu^-$	72.4	3	3.5 ± 0.2	63.8 ± 1.5
199.5	$\mu^+\mu^-$	81.8	0	3.9 ± 0.3	63.0 ± 1.5
201.6	$\mu^+\mu^-$	39.4	2	1.8 ± 0.2	62.5 ± 1.5
205.0	$\mu^+\mu^-$	69.1	0	3.0 ± 0.3	62.8 ± 1.5
206.5	$\mu^+\mu^-$	79.8	2	3.3 ± 0.3	62.1 ± 1.5
206.5U	$\mu^+\mu^-$	50.0	0	2.2 ± 0.2	56.9 ± 1.6
188.6	e^+e^-	153.8	4	7.9 ± 0.7	34.2 ± 1.3
191.1	e^+e^-	24.5	1	1.2 ± 0.2	40.8 ± 1.6
195.5	e^+e^-	72.4	4	4.7 ± 0.5	45.3 ± 1.6
199.5	e^+e^-	81.8	5	4.1 ± 0.4	45.2 ± 1.6
201.6	e^+e^-	39.4	1	1.9 ± 0.2	45.1 ± 1.6
205.0	e^+e^-	69.1	3	3.6 ± 0.3	44.8 ± 1.6
206.5	e^+e^-	79.8	1	4.0 ± 0.4	42.9 ± 1.6
206.5U	e^+e^-	50.0	1	2.3 ± 0.3	39.9 ± 1.6
188.6	$\tau^+\tau^-$	153.8	7	9.4 ± 0.8	21.4 ± 1.4
191.1	$\tau^+\tau^-$	24.5	1	1.9 ± 0.2	17.3 ± 1.4
195.5	$\tau^+\tau^-$	72.4	7	5.7 ± 0.6	20.2 ± 2.1
199.5	$\tau^+\tau^-$	81.8	10	6.3 ± 0.6	27.3 ± 1.5
201.6	$\tau^+\tau^-$	39.4	2	3.3 ± 0.4	28.2 ± 1.5
205.0	$\tau^+\tau^-$	69.1	5	5.7 ± 0.6	29.5 ± 1.5
206.5	$\tau^+\tau^-$	79.8	3	7.1 ± 0.7	30.3 ± 1.5
206.5U	$\tau^+\tau^-$	50.0	2	4.5 ± 0.4	29.5 ± 1.5

Table 8. Integrated luminosity, observed number of events, expected number of background events and signal efficiency ($60\,\mathrm{GeV}/c^2$ signal mass) for different energies in the low mass analysis. The last lines of each channel (206.5U) refers to the data taken with one TPC sector inoperative, which has been fully taken into account in the event simulations. Systematic and statistical errors are combined in quadrature

$\sqrt{s}$ (GeV)	Channel	Luminosity (pb^{-1})	Data	Expected background	Signal efficiency (%)
188.6	$q\bar{q}$	152.4	58	51.5 ± 3.8	49.1 ± 1.6
191.6	$q\bar{q}$	24.7	6	10.1 ± 0.5	50.0 ± 1.7
195.5	$q\bar{q}$	74.3	36	31.3 ± 1.6	49.6 ± 1.7
199.5	$q\bar{q}$	82.2	37	44.3 ± 2.3	50.5 ± 1.7
201.6	$q\bar{q}$	40.0	10	12.0 ± 0.6	44.2 ± 1.7
205.0	$q\bar{q}$	74.3	26	26.2 ± 1.7	47.0 ± 1.5
206.5	$q\bar{q}$	82.8	30	33.4 ± 2.1	48.8 ± 1.5
206.5U	$q\bar{q}$	58.0	10	18.0 ± 1.2	43.6 ± 1.5

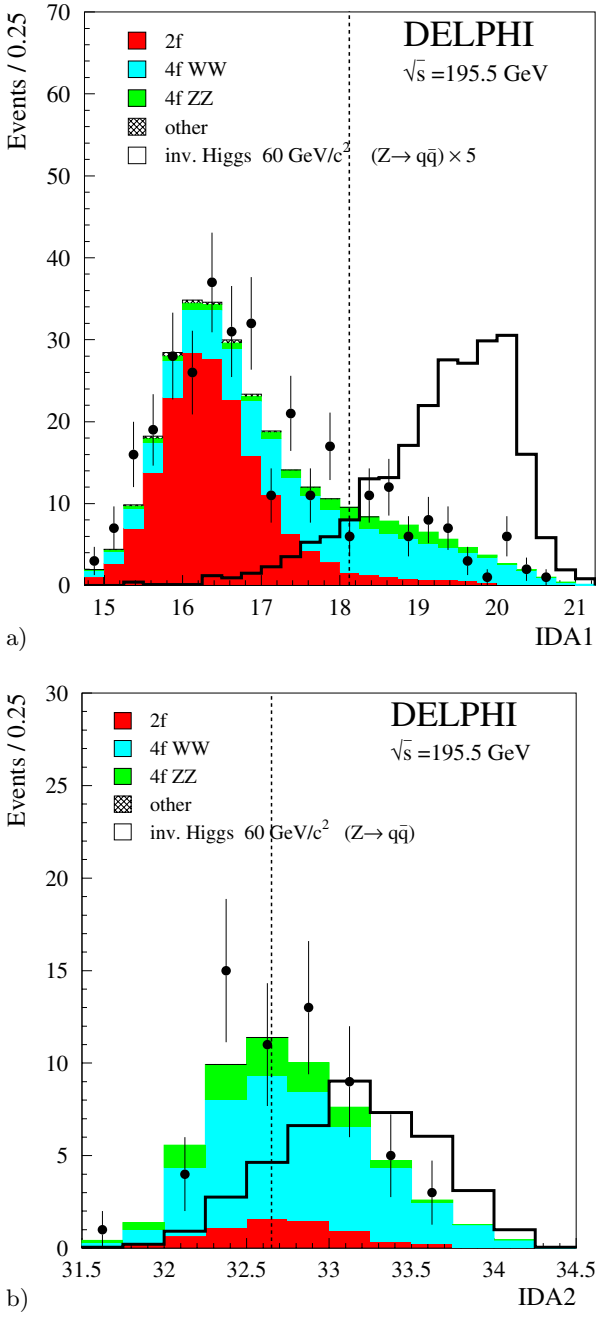

Fig. 6a,b. Hadronic channel low mass analysis: Distributions for the IDA variables after first **a** and second IDA step **b** at $\sqrt{s}$=195.5 GeV. The dashed line indicates the cut on the IDA variable. The white histogram shows the expectation of a 60 GeV/c^2 Higgs signal where the signal rate is enhanced by a factor 5 for **a**

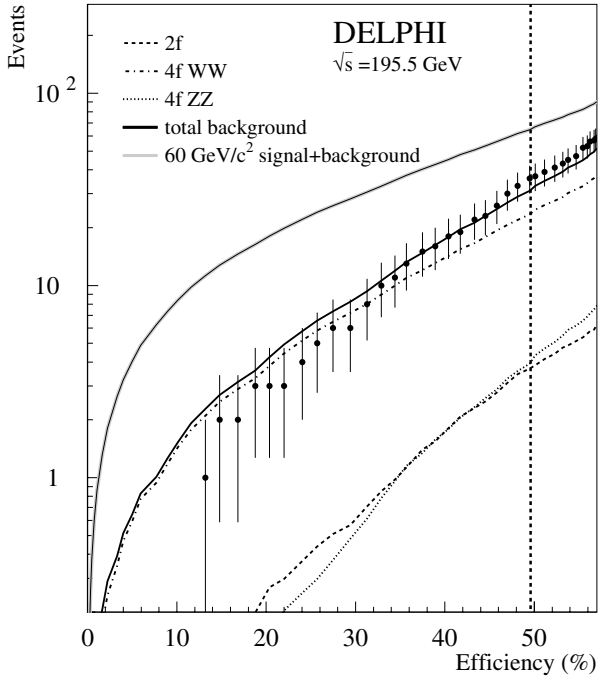

Fig. 7. Hadronic channel low mass analysis: Data and expected background for the 195.5 GeV centre-of-mass energy as a function of the efficiency for an invisibly decaying Higgs boson of 60 GeV/c^2. The lines show number of events from the most important background reactions and the solid black line shows the sum of all the background processes. In addition the grey line shows the expectation for a 60 GeV/c^2 Higgs signal added on top of the background. The vertical dashed line indicates the final cut chosen to maximise the sensitivity

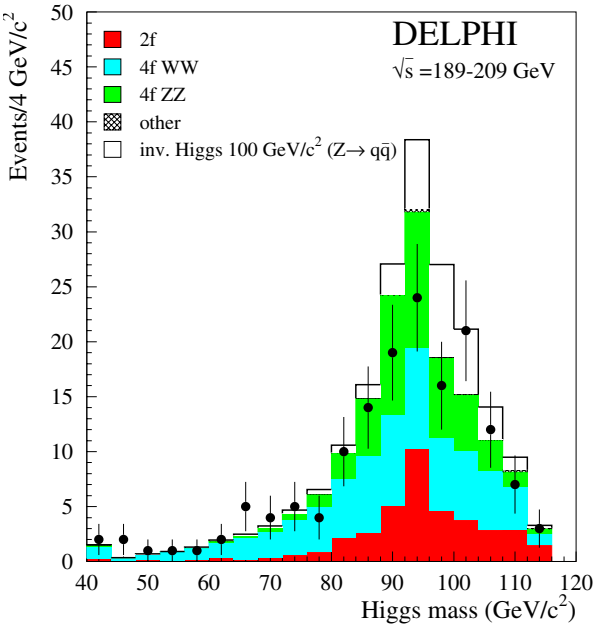

Fig. 8. Hadronic channel high mass analysis: Reconstructed Higgs boson mass for $\sqrt{s}$ from 189 to 209 GeV after the final selection. The white histogram corresponds to a Higgs boson with 100 GeV/c^2 mass decaying with a branching fraction of 100% into invisible modes

This resulted in slightly smaller integrated luminosities than for the hadronic search channel. An initial set of cuts was applied to select a sample enriched in leptonic events. A total charged-particle multiplicity between 2 and 5 was required. All particles in the event were clustered into jets using the LUCLUS algorithm [26] ($d_{\mathrm{join}} = 6.5\,\mathrm{GeV}/c$) and only events with two reconstructed jets were retained. Both

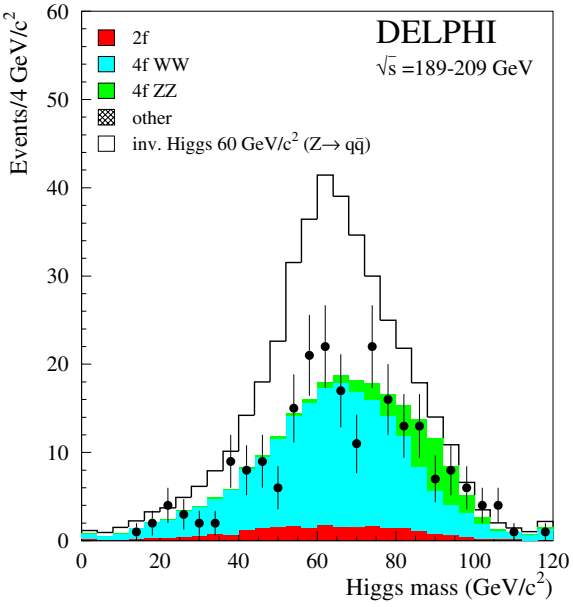

Fig. 9. Hadronic channel low mass analysis: Reconstructed Higgs boson mass for $\sqrt{s}$ from 189 to 209 GeV after the final selection. The white histogram corresponds to a Higgs boson with 60 GeV/c^2 mass decaying with a branching fraction of 100% into invisible modes

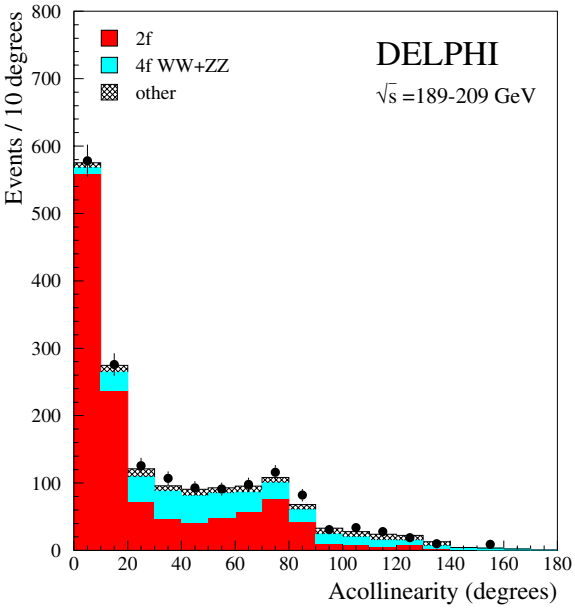

Fig. 10. Leptonic channels: Acollinearity distribution for $\sqrt{s}$ from 189 to 209 GeV after the preselection

jets had to contain at least one charged particle and at least one jet had to contain exactly one charged particle.

In order to reduce the background from two-photon collisions and radiative di-lepton events, the acoplanarity, $\theta_{\rm acop}$, had to be larger than 2°, and the acollinearity, $\theta_{\rm acol}$, had to be larger than 3°. In addition, the total momentum transverse to the beam direction, $p_{\rm T}$, had to exceed $0.02\sqrt{s}/c$. Finally, the energy of the most energetic photon was required to be less than $0.15\sqrt{s}$. The angle between that photon and the charged system projected onto the plane perpendicular to the beam axis had to be less than 170°. The agreement of data and background at the preselection level is shown in Fig. 10 for all data sets.

4.2 Channel identification

For the preselected events, jets were then identified as either μ, e or τ and two leptons with the same flavour were required. Owing to the low level of background, the three lepton identifications rely on loose criteria. A charged particle was identified as a muon if at least one hit in the muon chambers was associated to it, or if it had energy deposited in the outermost layer of the hadron calorimeter. In addition, the energy deposited in the other layers had to be compatible with that from a minimum ionising particle. Only jets with exactly one charged particle were tagged as muons. For the identification of a charged particle as an electron the energies deposited in the electromagnetic calorimeters, in the different layers of the hadron calorimeter, and in addition the energy loss in the Time Projection Chamber were used. An electron jet had to contain a maximum of two charged particles with at least one identified electron. A lepton was defined as a cascade decay coming from a τ if the momentum was lower than $0.13\sqrt{s}/c$. In this case the charged particle is no longer classified as a muon or as an electron. If no muon or electron was identified, the particle was considered a hadron from a τ decay. Thus, there is no overlap between the event samples selected in the three channels. The number of data and simulated background events are given in Table 6 for each centre-of-mass energy. A detailed description of the lepton identification is given in [28].

4.3 Channel-dependent criteria

After the preselection, different cuts were applied in each channel in order to reduce the remaining background. The optimisation of the efficiency has been performed separately for mass ranges of 50 to 85 GeV/c^2 and 85 to 115 GeV/c^2.

In the $\mu^+\mu^-$ channel only events with exactly two charged particle tracks were accepted. The direction of the missing momentum had to deviate from the beam axis by more that 18° in order to reject $\rm Z \to \mu^+\mu^-(\gamma)$ and $\gamma\gamma \to \mu^+\mu^-$ processes. The di-muon mass was required to be between 75 GeV/c^2 and 97.5 GeV/c^2, to be consistent with the Z boson mass. After that, two different sets of cuts were applied depending on the reconstructed Higgs boson mass as defined in Sect. 4.5. If the reconstructed mass was higher than 85 GeV/c^2 the momentum of the most energetic muon had to be between $0.2\sqrt{s}/c$ and $0.4\sqrt{s}/c$. Furthermore, $E_{\rm vis} < 0.55\sqrt{s}$, $p_{\rm T} < 0.25\sqrt{s}/c$ and $\theta_{\rm acol} < 60°$ was required. Otherwise, the momentum of the most energetic muon had to be between $0.25\sqrt{s}/c$ and $0.45\sqrt{s}/c$, and $0.45\sqrt{s} < E_{\rm vis} < 0.65\sqrt{s}$, $p_{\rm T} < 0.4\sqrt{s}/c$ and $45° < \theta_{\rm acol} < 85°$ was required. The mass resolution for $\rm Z \to \mu^+\mu^-$ is about 4.5 GeV/c^2.

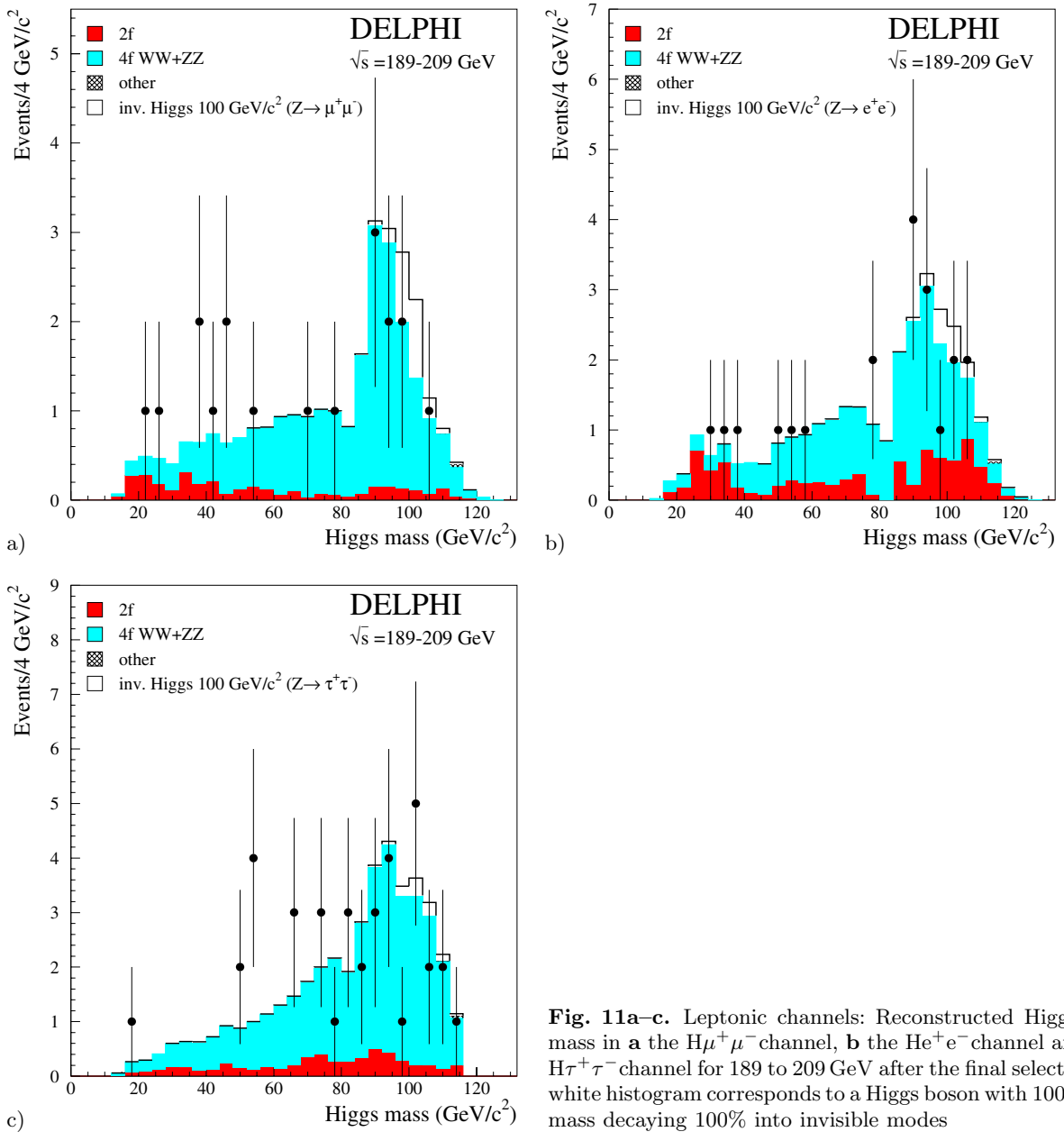

Fig. 11a–c. Leptonic channels: Reconstructed Higgs boson mass in **a** the $\mathrm{H}\mu^+\mu^-$channel, **b** the $\mathrm{He^+e^-}$channel and **c** the $\mathrm{H}\tau^+\tau^-$channel for 189 to 209 GeV after the final selection. The white histogram corresponds to a Higgs boson with 100 GeV/c^2 mass decaying 100% into invisible modes

In the $\mathrm{e^+e^-}$ channel a maximum of four tracks were required. The most important background arises from radiative Bhabha scattering and $\mathrm{Ze^+e^-}$ events. To suppress these backgrounds, the direction of the missing momentum and the polar angle of both leptons had to deviate from the beam axis by more than 18°, the transverse energy had to be greater than $0.15\sqrt{s}$ and the neutral electromagnetic energy had to be less than $0.1\sqrt{s}$. The invariant mass of the two leptons had to be between 75 GeV/c^2 and 100 GeV/c^2 to be consistent with the Z boson mass. The mass resolution for $\mathrm{Z} \to \mathrm{e^+e^-}$ is about 5.7 GeV/c^2. Then, if the mass reconstructed was higher than 85 GeV/c^2, the momentum of the most energetic electron had to be lower than $0.35\sqrt{s}$, and the total associated energy was required to be less than $0.55\sqrt{s}$, $p_\mathrm{T} < 0.25\sqrt{s}/c$ and $\theta_\mathrm{acol} < 60°$. Otherwise, the momentum of the most energetic electron had to be between $0.25\sqrt{s}/c$ and $0.45\sqrt{s}/c$, and the total associated energy was required to be less than $0.65\sqrt{s}$. In addition, the selection $p_\mathrm{T} < 0.4\sqrt{s}/c$ and $45° < \theta_\mathrm{acol} < 85°$ was applied.

In the $\tau^+\tau^-$ channel tighter cuts were applied on the acoplanarity and acollinearity in order to reduce the remaining backgrounds from $\tau^+\tau^-(\gamma)$ and $\gamma\gamma \to \ell\ell$ processes. The invariant mass of both jets had to be less than 3 GeV/c^2. In addition, the transverse energy had to be greater than $0.1\sqrt{s}$, the visible energy of all particles with $|\cos\theta| < 0.9$ had to be greater than $0.06\sqrt{s}$ and the energy of both jets had to be less than $0.26\sqrt{s}$. Finally, if the mass reconstructed was higher than 85 GeV/c^2, the acollinearity had to be between 10° and 60°, otherwise, it had to be between 45° and 85°. No cut on the reconstructed mass

is applied because of the large missing energy from the associated neutrinos.

4.4 Systematic uncertainties

Several sources of systematic uncertainties were investigated for their effect on the signal efficiency and the background rate. The particle identification method was checked with di-lepton samples both at Z peak and high energy, and the simulation and data rates were found to agree within ±1%. The modelling of the preselection variables agrees within statistical errors with the data. The track selection and the track reconstruction efficiency were also taken into account in the total systematic error. The effects of detector miscalibration and deficiencies were investigated using $\mu^+\mu^-\gamma$ or $e^+e^-\gamma$ events, where the lepton energies are determined directly and recoiling from the photon. The comparison between data and simulation rate was found to be better than ±1%. Additional systematic effects were estimated by comparing the data collected, at the Z peak, during the period with one TPC sector inoperative with simulation samples produced with the same detectors conditions. The total systematic error on the signal efficiency was ±1.1%. The total systematic error on the background rate was up to 10%. The total systematic error and statistical error from the limited MC statistics are combined in quadrature and given in Table 7.

4.5 Mass reconstruction

The mass of the invisibly decaying particle was computed from the measured energies assuming momentum and energy conservation. To improve the resolution a χ^2 fit was applied constraining the visible mass to be compatible with a Z boson. In the case of the $\tau^+\tau^-$ channel, the measured four-momenta of the decay products do not reproduce correctly the τ energy. Therefore, the mass was calculated under the assumption that both τ leptons had the same energy and the τ neutrino went along the direction of the τ lepton. This, together with the visible mass constraint, allowed an estimation of the τ energy and of the invisible mass. The invisible mass for the candidates as well as for the expected background from Standard Model processes for the different channels is shown in Fig. 11.

5 Results

A comparison of the observed and predicted numbers of selected events for the four channels is summarised in Table 7 and 8. The agreement between the data and the SM prediction is good for all channels and no indication for a Higgs boson decaying into invisible particles has been observed. The signal efficiencies of the four channels are shown in Fig. 12 as a function of the Higgs mass for $\sqrt{s} = 206.5$ GeV.

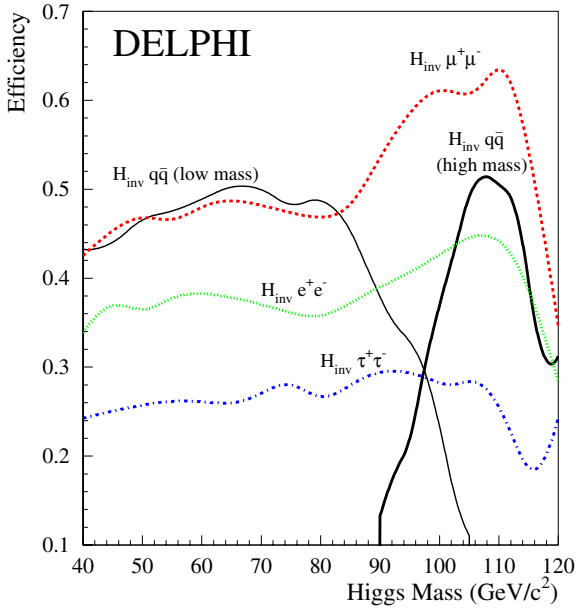

Fig. 12. Efficiencies for the Higgs boson masses between 40 and 120 GeV/c^2 for the different selection channels at $\sqrt{s} =$ 206.5 GeV

5.1 Model independent limits

The cross-section and mass limits were computed at the 95% CL with a likelihood method [29]. One-dimensional distributions of the reconstructed mass serve as input for the likelihood calculation. The impact of the correlation of the systematic errors is small and the limits result largely from the data taken at the higher centre-of-mass energies. More details about the confidence definition and computation can be found in [23]. All search channels and centre-of-mass energies were treated as separate experiments to obtain a likelihood function. In total 40 channels were evaluated as listed in Table 7 and 8, in addition to the $q\bar{q}$ channels from 161 and 172 GeV data [7], and the $q\bar{q}$ and $\mu^+\mu^-$ channels from 183 GeV data [8]. In order to address the overlap between the low and high mass analyses in the hadronic channel, the expected performance was calculated for both analyses in the overlap region. At each test mass the analysis with the best expected exclusion power was then chosen for the calculation of the limit.

No indication of a signal is observed above the background expectation. This is shown in Fig. 13 which displays the curves of the confidence levels in the background hypothesis, CL_b, as a function of the Higgs boson mass hypothesis, for the hadron and lepton channels separately. Over most of the range of masses the agreement between data and the background expectations is within one standard deviation. However, at a few masses in the muon and electron channels, there are disagreements near or slightly above two standard deviations, which are due to deficits of data in several bins of the reconstructed mass spectra in these channels, as shown in Fig. 11. Figure 14 displays the observed and expected upper limits on the cross-section for the process $e^+e^- \to Z(\text{anything})H(\text{invisible})$ as a function of the Higgs boson mass. From the compar-

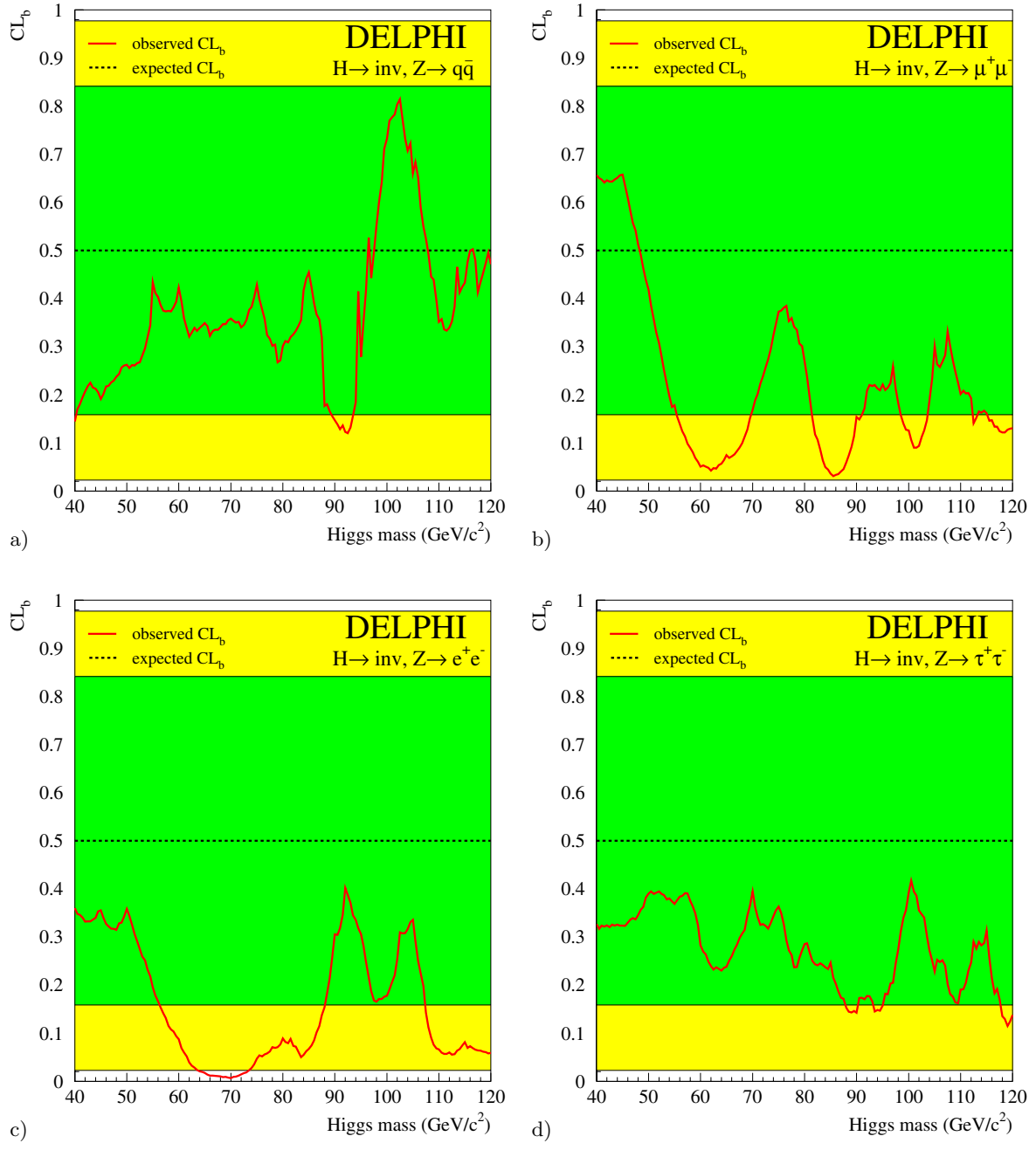

Fig. 13a–d. Confidence levels for the different decay channels as a function of the Higgs mass. Shown are the observed (solid) and expected (dashed) confidences for the background-only hypothesis in the Hq$\bar{\text{q}}$ **a**, H$\mu^+\mu^-$ **b**, He^+e^- **c** and H$\tau^+\tau^-$ **d** channels. The dark grey band corresponds to the 68.3% expected confidence interval and the light grey band to the 95.0% confidence interval. The structures near 94 and 96 GeV in plot **a** are due to the switching from the low-mass to the high-mass optimization in the hadronic channel

ison with the Standard Model (SM) Higgs boson cross-section the observed (expected median) mass limits are 112.1 (110.5) GeV/c^2 for the Higgs boson decaying into invisible particles.

In a model-independent approach the branching ratio into invisible particles BR_{inv} can be considered a free parameter. The remaining decay modes are then visible and are assumed to follow the SM decay probabilities. In this case the searches for visible and invisible Higgs boson decays can be combined to determine the excluded region in the BR_{inv} versus m_H plane assuming SM production cross-sections. Using the DELPHI data from the SM Higgs searches [7, 23, 30–32] a lower mass limit of 111.8 GeV/c^2 can be set independently of the hypothesis on the fraction of invisible decay modes, as shown in Fig. 15. In computing these limits, the overlap between the standard H$\nu\bar{\nu}$ and the invisible Higgs boson hadronic selections have

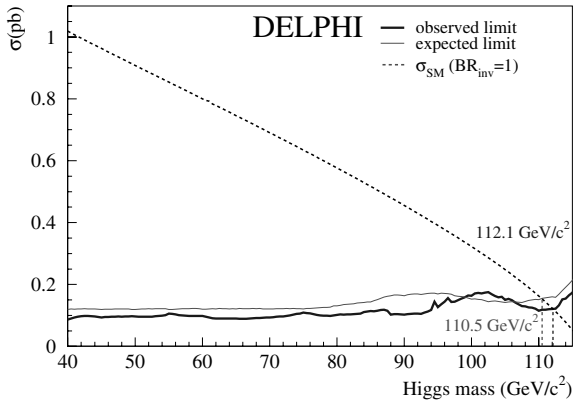

Fig. 14. The 95% CL upper limit on the cross-section $e^+e^- \to$ Z(anything) H(invisible) as a function of the Higgs boson mass. The dashed line shows the standard model cross-section for the Higgs boson production with $BR_{\rm inv} = 1$

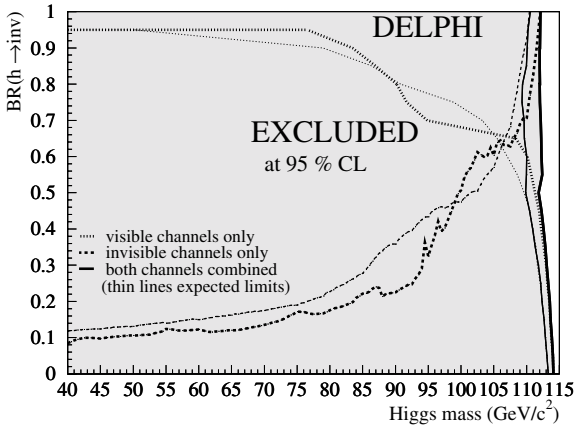

Fig. 15. The Higgs boson mass limits as a function of the branching ratio into invisible decays $BR_{\rm inv}$, assuming a $1 - BR_{\rm inv}$ branching ratio into standard visible decay modes

not been used, conservatively for the limit, by omitting the $H\nu\bar{\nu}$ ($H_{inv}q\bar{q}$) results in the region $BR_{\rm inv} > 50\%(< 50\%)$.

5.2 Limits for a Majoron model

The limits computed above can be used to set a limit on the Higgs bosons in a Majoron model [4–6] with one complex doublet ϕ and one complex singlet η. Mixing of the real parts of ϕ and η leads to two massive Higgs bosons:

$$H = \phi_R \cos\theta - \eta_R \sin\theta$$
$$S = \phi_R \sin\theta + \eta_R \cos\theta$$

where θ is the mixing angle. The imaginary part of the singlet is identified as the Majoron. The Majoron is decoupled from the fermions and gauge bosons, but might have a large coupling to the Higgs bosons. In this model the free parameters are the masses of H and S, the mixing angle θ and the ratio of the vacuum expectation values of the two fields ϕ and η ($\tan\beta \equiv \frac{v_\phi}{v_\eta}$). The production rates of the H and S are reduced with respect to the SM Higgs boson, by factors of $\cos^2\theta$ and $\sin^2\theta$, respectively. The decay

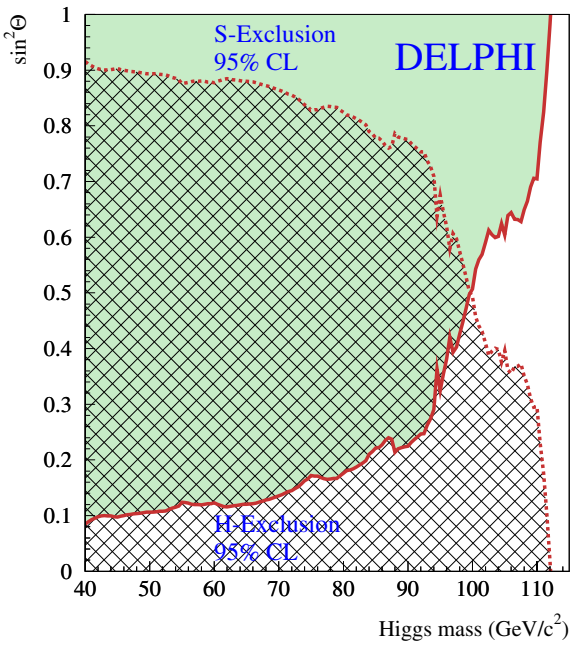

Fig. 16. Limit on $\sin^2\theta$ as a function of the Higgs boson mass at 95% CL. S and H are the Higgs bosons in the Majoron model. The grey region is excluded for the S Higgs boson and the hatched region for the H Higgs boson. The massive Higgs bosons decay almost entirely into invisible Majoron pairs for large $\tan\beta$ values

widths of the H and S into the heaviest possible fermion-antifermion pair are reduced by the same factor and their decay widths into a Majoron pair are proportional to the complementary factors ($\cos^2\theta$ for S and $\sin^2\theta$ for H). The HZ and SZ cross-section times branching ratio into invisible decays is calculated and compared to the excluded cross-section of Sect. 5.1. In the case where the invisible Higgs boson decay mode is dominant ($\tan\beta$ larger than about 10), the excluded region in the mixing angle versus Higgs boson mass plane is shown in Fig. 16.

5.3 Limits in the MSSM

In the MSSM, there are parameter regions where the Higgs boson can decay into neutralinos, $\tilde{\chi}^0$, which leads to invisible Higgs decays. As an illustration a benchmark scenario including such decays was defined from the so-called "m_h-max scenario" [23]. In this scenario the MSSM parameters are the mass of the pseudoscalar Higgs boson, m_A, the ratio of the vacuum expectation values, $\tan\beta$, the mixing in the scalar top sector X_t, the gaugino mass M_2 and the Higgs self-coupling μ. M_2 and μ were modified to obtain light neutralino masses setting $M_2 = \mu = 150\,\mathrm{GeV}/c^2$. Then a scan was performed in the $\tan\beta$-m_A plane. For each scan point the hZ production cross-section and the Higgs boson branching ratio into neutralinos were calculated, and the point was considered as excluded if the product was found to be larger than the excluded cross-section as shown in Fig. 14. Figure 17 shows the excluded region from the search

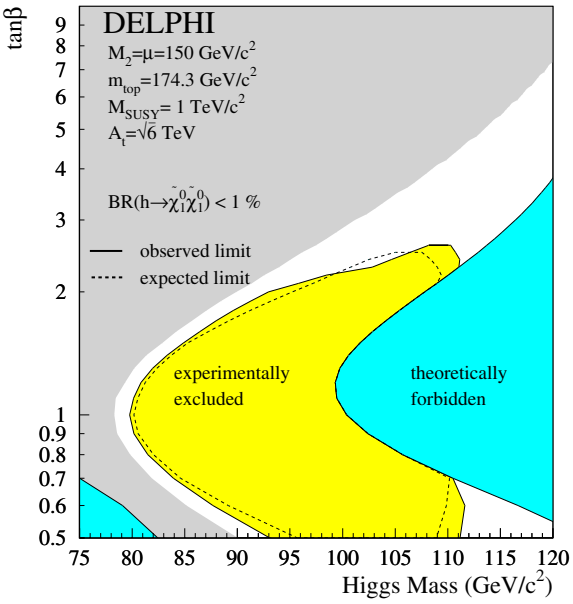

Fig. 17. Excluded region in the MSSM from searches for a Higgs boson decaying into invisible final states for the modified "m_h-max scenario" described in the text. The different grey areas show the theoretically forbidden region (dark), the region where the Higgs boson does not decay into neutralinos (intermediate), the region which is excluded at 95% CL by this search for invisibly decaying Higgs bosons (light) and the unexcluded region (white)

for invisible Higgs decays, the theoretically forbidden region, and the region where the branching ratio $h \to \tilde{\chi}^0\tilde{\chi}^0$ is less than 1%. In this benchmark scenario, the invisible Higgs boson search covers a large region in the low $\tan\beta$ regime. The white regions cannot be excluded by the invisible Higgs searches alone because the branching ratio into neutralinos is too small. The search for the invisible Higgs boson decays also sets limits in the general framework searches for Supersymmetric particles [33] and for searches in Anomaly Mediated Supersymmetry Breaking (AMSB) models [34].

6 Conclusion

In the data samples collected by the DELPHI detector at centre-of-mass energies from 189 to 209 GeV, 153 $q\bar{q}$ (213 for the low mass analysis), 18 $\mu^+\mu^-$, 20 e^+e^- and 37 $\tau^+\tau^-$ events were selected in searches for a Higgs boson decaying into invisible final states. These numbers are consistent with the expectation from SM background processes.

We set a 95% CL lower mass limit of 112.1 GeV/c^2 for Higgs bosons with a Standard Model cross-section and with 100% branching fraction into invisible decays. Excluded parameter regions are given in a simple Majoron model. The invisible Higgs boson search is important to cover some parameter regions in the MSSM where Higgs decays into neutralinos are kinematically allowed.

Acknowledgements. We are greatly indebted to our technical collaborators, to the members of the CERN-SL Division for the excellent performance of the LEP collider, and to the funding agencies for their support in building and operating the DELPHI detector. We acknowledge in particular the support of Austrian Federal Ministry of Education, Science and Culture, GZ 616.364/2-III/2a/98, FNRS-FWO, Flanders Institute to encourage scientific and technological research in the industry (IWT), Federal Office for Scientific, Technical and Cultural affairs (OSTC), Belgium, FINEP, CNPq, CAPES, FUJB and FAPERJ, Brazil, Czech Ministry of Industry and Trade, GA CR 202/99/1362, Commission of the European Communities (DG XII), Direction des Sciences de la Matière, CEA, France, Bundesministerium für Bildung, Wissenschaft, Forschung und Technologie, Germany, General Secretariat for Research and Technology, Greece, National Science Foundation (NWO) and Foundation for Research on Matter (FOM), The Netherlands, Norwegian Research Council, State Committee for Scientific Research, Poland, SPUB-M/CERN/PO3/DZ296/2000, SPUB-M/CERN/PO3/DZ297/2000 and 2P03B 104 19 and 2P03B 69 23(2002–2004) JNICT-Junta Nacional de Investigação Científica e Tecnológica, Portugal, Vedecka grantova agentura MS SR, Slovakia, Nr. 95/5195/134, Ministry of Science and Technology of the Republic of Slovenia, CICYT, Spain, AEN99-0950 and AEN99-0761, The Swedish Natural Science Research Council, Particle Physics and Astronomy Research Council, UK, Department of Energy, USA, DE-FG02-01ER41155, EEC RTN contract HPRN-CT-00292-2002.

References

1. A. Djouadi, P. Janot, J. Kalinowski and P.M. Zerwas, Phys. Lett. B **376**, 220 (1996)
2. T. Binoth and J.J. van der Bij, Z. Phys. C **75**, 17 (1997)
3. K. Belotsky et al., Invisible Higgs boson decay into massive neutrinos of fourth generation, hep-ph/0210153
4. Y. Chikashige, R.N. Mohapatra, R.D. Peccei, Phys. Lett. B **98**, 265 (1981); R.E. Shrock, M. Suzuki, Phys. Lett. B **110**, 250 (1982); R.N. Mohapatra, J.W.F. Valle, Phys. Rev. D **34**, 1642 (1986); M.C. Gonzalez-Garcia, J.W.F. Valle, Phys. Lett. B **216**, 360 (1989); E.D Carlson, L.J. Hall, Phys. Rev. D **40**, 3187 (1989); L.F. Li,Y. Liu, L. Wolfenstein, Phys. Lett. B **159**, 45 (1985); A. Zee, Phys. Lett. B **93**, 389 (1980)
5. F. de Campos et al., Phys. Rev. D **55**, 1316 (1997)
6. S.P. Martin and J.D. Wells,Phys. Rev. D **60**, 035006 (1999)
7. DELPHI Collaboration, P. Abreu et al., Eur. Phys. J. C **2**, 1 (1998)
8. DELPHI Collaboration, P. Abreu et al., Phys. Lett. B **459**, 367 (1999)
9. ALEPH Collaboration, A. Heister et al. Phys. Lett. B **526**, 191 (2002)
10. L3 Collaboration, M. Acciarri et al., Phys. Lett. B **485**, 85 (2000)
11. DELPHI Collaboration, P. Abreu et al., Nucl. Instrum. Methods A **378**, 57 (1996); DELPHI Collaboration, P. Aarnio et al, Nucl. Instrum. Methods A **303**, 233 (1991)
12. DELPHI Silicon Tracker Group, P. Chochula et al., Nucl. Instrum. Methods A **412**, 304 (1998)
13. P. Janot, in CERN Report 96-01, Vol. 2, p. 309
14. S. Jadach, B.F.L. Ward and Z. Was, Comput. Phys. Commun. **130**, 260 (2000)

15. S. Jadach, W. Placzek and B.F.L. Ward, Phys. Lett. B **390**, 298 (1997)
16. E. Accomando and A. Ballestrero, Comput. Phys. Commun. **99**, 270 (1997); E. Accomando, A. Ballestrero and E. Maina, Comput. Phys. Commun. **150**, 166 (2003)
17. T. Sjöstrand, Comput. Phys. Commun. **39**, 347 (1986); Comput. Phys. Commun. **82**, 74 (1994)
18. F.A. Berends, P.H. Daverveldt, R. Kleiss, Nucl. Phys. **253**, 421 (1985); Comput. Phys. Commun. **40**, 271, 285 and 309 (1986)
19. S. Jadach, B.F.L Ward and Z. Was, Comput. Phys. Commun. **79**, 503 (1994)
20. S. Catani et al., Phys. Lett. B **269**, 432 (1991)
21. T.G.M. Malmgren, Comput. Phys. Commun. **106**, 230 (1997); T.G.M. Malmgren and K.E. Johansson, Nucl. Instrum. Methods A **403**, 481 (1998)
22. DELPHI Collaboration, P. Abreu et al., Phys. Lett. B **372**, 172 (1996)
23. DELPHI Collaboration, J. Abdallah et al., Final results on SM and MSSM Neutral Higgs bosons, CERN EP/2003-008, Eur. Phys. J (accepted)
24. L. Lönnblad, Comput. Phys. Commun. **71**, 15 (1992)
25. M. W. Grünewald et al., In CERN Report 2000-009 p. 1–135. Four-fermion production in electron positron collisions.
26. T. Sjöstrand, PYTHIA 5.7 / JETSET 7.4, CERN-TH.7112/93 (1993)
27. DELPHI Collaboration, J. Abdallah et al., ZZ production in e^+e^- interactions at $\sqrt{s}$ = 183–209 GeV, CERN EP/2003-009, Eur. Phys. J (accepted)
28. DELPHI Collaboration, P. Abreu et al., Phys. Lett. B **511**, 159 (2001)
29. A.L. Read, in CERN Report 2000-005 p. 81 (2000)
30. DELPHI Collaboration, P. Abreu et al., Eur. Phys. J. C **10**, 563 (1999)
31. DELPHI Collaboration, P. Abreu et al., Eur. Phys. J. C **17**, 187 (2000)
32. DELPHI Collaboration, J. Abdallah et al., Eur. Phys. J. C **23**, 409 (2002)
33. DELPHI Collaboration, J. Abdallah et al., Searches for Supersymmetric particles in e^+e^- collisions up to 208 GeV and interpretation of the results within the MSSM, CERN-EP/2003-007, Eur. Phys. J. C (accepted)
34. DELPHI Collaboration, J. Abdallah et al., Study of the Anomaly Mediated SUSY Breaking Model in DELPHI, CERN-EP/2003-048, and Eur. Phys. J. C (submitted)